Mechanofluorophores Hot Paper

How to cite: *Angew. Chem. Int. Ed.* **2021**, *60*, 13287–13293
International Edition: doi.org/10.1002/anie.202101716
German Edition: doi.org/10.1002/ange.202101716

Multicolor Mechanofluorophores for the Quantitative Detection of Covalent Bond Scission in Polymers

*Christoph Baumann, Maria Stratigaki, Silvia P. Centeno, and Robert Göstl**

Abstract: *The fracture of polymer materials is a multiscale process starting with the scission of a single molecular bond advancing to a site of failure within the bulk. Quantifying the bonds broken during this process remains a big challenge yet would help to understand the distribution and dissipation of macroscopic mechanical energy. We here show the design and synthesis of fluorogenic molecular optical force probes (mechanofluorophores) covering the entire visible spectrum in both absorption and emission. Their dual fluorescent character allows to track non-broken and broken bonds in dissolved and bulk polymers by fluorescence spectroscopy and microscopy. Importantly, we develop an approach to determine the absolute number and relative fraction of intact and cleaved bonds with high local resolution. We anticipate that our mechanofluorophores in combination with our quantification methodology will allow to quantitatively describe fracture processes in materials ranging from soft hydrogels to high-performance polymers.*

Introduction

The deterioration or fracture of materials submitted to mechanical force is a molecular process progressing into a macroscopic site of failure. Understanding such multiscale phenomena is a nontrivial endeavor and hence requires the development of advanced analytical tools. In macromolecular materials, mechanical force beyond a certain threshold ultimately leads to the scission of covalent bonds and hence the qualitative and quantitative observation of this process is a promising strategy to tackle this challenge. Molecules that undergo productive bond scission upon the application of mechanical force (mechanophores), particularly those altering their optical properties, show potential in this context and are hence investigated as force reporting probes in polymer materials.[1–3] Notable representatives of these are spiro(thio)pyran[4–8] and its rhodamine derivatives,[9–11] dioxetane,[12–14] persistent delocalized radicals,[15–18] and aggregachromic dyes.[19–21] However, the direct correlation of macroscopic deformation with microscopic and molecular events is still challenging, yet fundamental in the field of polymer science. Recently, initial steps have been taken to address this challenge by using confocal laser scanning microscopy (CLSM) in combination with fluorogenic mechanophores to quantitatively describe the spatial distribution of stress, strain, and mechanical energy dissipation within hydrogels[22,23] and elastomers.[24] However, these approaches are limited by either a complicated relationship between fluorescence signal and the number of broken bonds[22] or a lack of feedback over the number of intact bonds.[23,24]

Here we report a new mechanofluorophore design that allows tuning of excitation and emission wavelengths and is fluorescent in its deactivated as well as its activated state[11,25] with a large spectral separation between these states. The nature of this fluorogenic mechanophore platform renders the quantitative detection of bond scission by CLSM possible with high spatial resolution. We use Diels–Alder (DA) adducts[26–28] of π-extended anthracenes and maleimide as the mechanoresponsive moiety because the alteration of their fluorescence is detectable at low concentrations and independent of time (Scheme 1a).[23,24,29–31] For this, we show the synthesis of three new mechanofluorophores based on a symmetric design (Scheme 1b): Firstly, we approximate the conventional non-symmetric 9-π-extended anthracene mechanophore **I**[29,30] with a central phenyl moiety **a** to prove the working principle of the new design concept. We then introduce dual fluorescent character by synthesizing acenothiadiazole-based mechanofluorophores bearing either a benzo[*c*][1,2,5]-thiadiazole (BTD, **b**) or naphtho[2,3-*c*]-[1,2,5]thiadiazole (NTD, **c**) central moiety. These acenothiadiazoles not only show a considerable bathochromic shift in their excitation and emission wavelengths, but moreover allow direct quantification of covalent bond scission events at the fracture site. The mechanofluorophores are incorporated into linear poly(methyl acrylate) (PMA) and crosslinked poly(hexyl methacrylate) (PHMA) networks. The successful force-induced retro DA reaction is confirmed in solution on linear PMA chains via ultrasound irradiation and in the solid state on fractured PHMA rubber networks. For the BTD mechanofluorophores in PHMA samples, we exemplarily

[*] C. Baumann, Dr. M. Stratigaki, Dr. S. P. Centeno, Dr. R. Göstl
DWI—Leibniz Institute for Interactive Materials
Forckenbeckstr. 50, 52056 Aachen (Germany)
E-mail: goestl@dwi.rwth-aachen.de
C. Baumann
Institute of Technical and Macromolecular Chemistry, RWTH Aachen University
Worringerweg 1, 52074 Aachen (Germany)
Dr. S. P. Centeno
Institute of Physical Chemistry, RWTH Aachen University
Landoltweg 2, 52074 Aachen (Germany)
Supporting information and the ORCID identification number(s) for the author(s) of this article can be found under: https://doi.org/10.1002/anie.202101716.

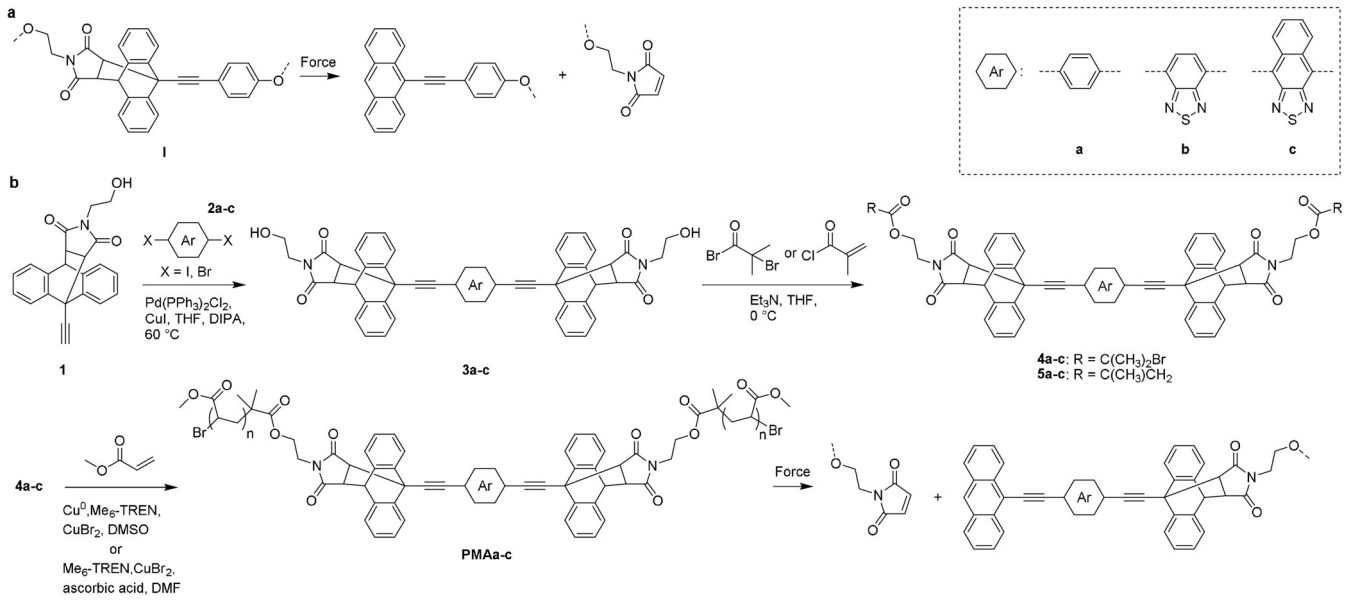

Scheme 1. DA adducts of π-extended anthracenes and maleimide undergo a force-induced retro DA reaction. a) Traditional non-symmetric mechanofluorophore design of previous work.[29,30] b) Synthetic pathway for modular, symmetric design of dual fluorescent mechanofluorophores in this work.

display the workflow for quantification of covalent bond scission via CLSM.

Results and Discussion

The mechanofluorophores were obtained starting from terminal alkyne **1**, the synthesis of which we described previously (Scheme 1b).[29,30] Subsequent Sonogashira-type cross-coupling with dihalide precursors of the desired central moiety **2a–c** yielded dialcohols **3a–c**. Depending on the desired polymerization technique, the dialcohols were then esterified either with α-bromoisobutyryl bromide to form the bifunctional initiators **4a–c** for controlled radical polymerization (CRP) or with methacryloyl chloride to yield crosslinkers **5a–c** for bulk free radical polymerization. Cu-catalyzed CRP of initiators **4a–c** gave linear telechelic polymer chains **PMAa** ($M_n = 52.3$ kDa, $Đ_M = 1.17$), **PMAb** ($M_n = 57.3$ kDa, $Đ_M = 1.20$), and **PMAc** ($M_n = 59.5$ kDa, $Đ_M = 2.15$) bearing the mechanofluorophores within their center (Figure S47–49). Incorporation of the mechanofluorophores as crosslinkers into bulk materials was performed by thermal bulk free radical polymerization of hexyl methacrylate with tetraethylene glycol dimethacrylate (TEGDMA) and **5a–c** to yield rubber networks **PHMAa–c**, respectively.

We anticipated that the new symmetric design would only lead to one retro DA reaction per mechanofluorophore under force even though two DA adduct moieties were present. This hypothesis was based on previous experiments that showed that a mechanophore is only active when positioned in the central region of the chain,[30] but not when in a terminal position,[32] as would be the case after one scission event occurred. To fully cover the visible spectrum with the available emission wavelengths, we introduced a phenyl, a BTD, and an NTD core, respectively. Both BTD and NTD are widely used chromophores for conjugated polymers and provide excellent π-conjugation and aromaticity.[33–38] To identify the activated mechanofluorophores, for determination of molar absorptivities and fluorescence quantum yields, and for concentration calibration for bond scission experiments using CLSM, control compounds **6a–c** (Figure S1) resembling the activated mechanofluorophores were synthesized.

The force-induced retro DA reactions of polymers **PMAa–c** were then investigated by irradiation with ultrasound using an immersion probe sonicator (20 kHz).[39] Sonication experiments were accompanied by gel permeation chromatography (GPC) via refractive index (RI) detector showing the expected decrease of the initial high molar mass signals and the emergence of new signals with ca. half of the initial molar mass with progressing sonication time (Figure 1a, S53, S55, S57). UV/Vis spectroscopy over the course of sonication revealed the emergence of bathochromically shifted absorption bands relative to the non-activated mechanophores. Notably, the absorption spectrum of **PMAa** after sonication was nearly identical to non-symmetrically activated **I**[29,30] with a slight bathochromic shift attributed to the additional alkyne moiety conjugated into the π-system (Figure 1b, S54). Excitation at a wavelength of 405 nm yielded the expected cyan fluorescence between 400–550 nm.

PMAb and **PMAc** were already fluorescent in their deactivated state and their spectral features were comparable to other alkynylated BTDs and NTDs reported in the literature.[40] **PMAb** before sonication revealed spectral characteristics analogous to the activated version of **PMAa** with cyan fluorescence. During sonication of **PMAb**, an absorption band at 455 nm emerged, approximately 75 nm redshifted compared to the non-activated form of the mechanophore (Figure 1c, S56). Fluorescence excitation at this band at a wavelength of 454 nm resulted in a yellow

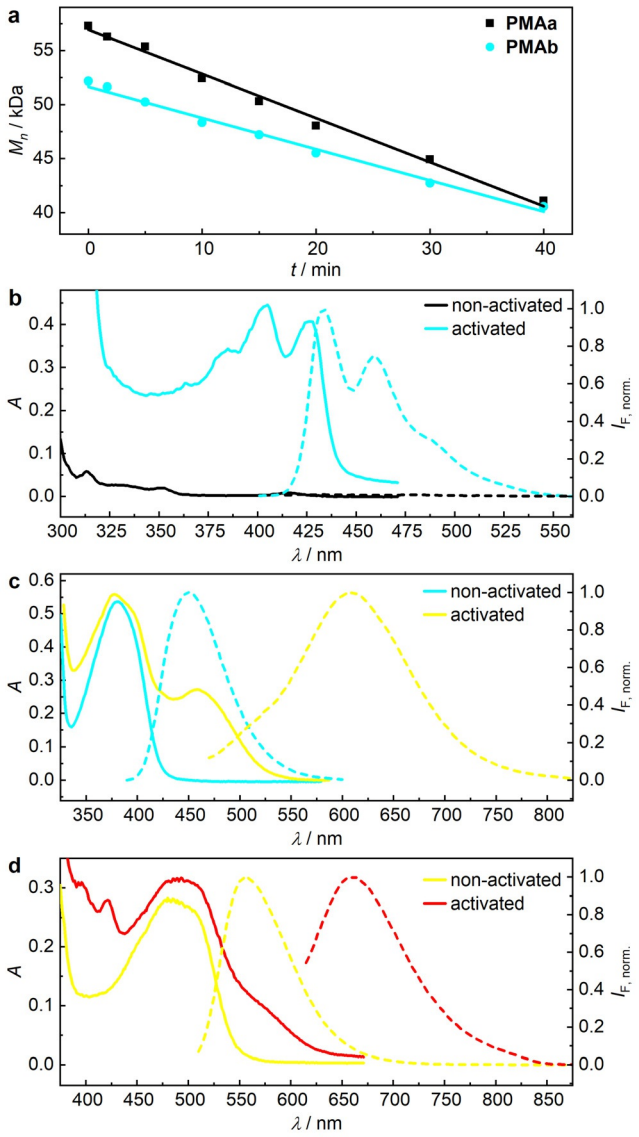

Figure 1. Sonochemical scission of polymers **PMAa–c**. a) Decrease of M_n over sonication time as determined by the RI detector of GPC elugrams including linear fits. Absorption (solid line) and emission spectra (dotted line) in MeCN before and after sonication of b) **PMAa** ($\lambda_{exc}=405$ nm), c) **PMAb** ($\lambda_{exc}=405$ and 454 nm), and d) **PMAc** ($\lambda_{exc}=495$ and 601 nm).

emission at 609 nm. **PMAc** was found to be even farther redshifted with an absorption band at 496 nm and yellow fluorescence at 558 nm in its deactivated form. Activation by sonication yielded a new absorption band at 552 nm while excitation at this band at the wavelength of 601 nm led to red emission at 659 nm (Figure 1d, S58).

Over the course of the sonication, the apparent scission rate constants k were determined from GPC but also from UV/Vis measurements via the molar absorptivities of control compounds **6a–c**.[41–43] Both approaches led to comparable values hinting towards a preferred chain scission at the mechanophore, however, slightly underestimating the rate constants by UV/Vis due to the insensitivity to non-specific chain scission (Figure S53–62). The apparent scission rate constants were calculated to $k_{\mathbf{PMAa},UV/Vis}=6.90\times10^{-3}\ min^{-1}$ and $k_{\mathbf{PMAb},UV/Vis}=4.42\times10^{-3}\ min^{-1}$. As we could not obtain a narrow disperse version of **PMAc**, scission rate constants could not be determined reliably for this mechanophore. Yet, together with the spectral features of the control compounds **6a–c** prepared for each activated mechanophore (Figure S50–52), these data strongly corroborate the successful and reasonably selective force-induced retro DA reaction at the center of the polymer chains where only one DA adduct moiety is cleaved and the second remains intact.

Fluorescence quantum yields were determined on small molecule initiators **4a–c** for the non-activated and control compounds **6a–c** for the activated state in MeCN using an Ulbricht sphere (Table S1 also for hexyl acetate and hexane). The phenyl mechanophore was only fluorescent in the activated state **6a** and showed a value of $\Phi_F=0.72$ ($\lambda_{exc}=405$ nm) that was comparable to the activated mechanophore **I**.[29] The dual fluorescent BTD mechanophore displayed an excellent quantum yield in the non-activated state **4b** of $\Phi_F=0.84$ ($\lambda_{exc}=405$ nm) whereas the force-activated derivative **6b** dropped to $\Phi_F=0.09$ ($\lambda_{exc}=457$ nm). A similar trend was observed for the NTD mechanophore where a good quantum yield in the non-activated state **4c** of $\Phi_F=0.50$ ($\lambda_{exc}=496$ nm) was measured, but a low quantum yield of $\Phi_F=0.02$ ($\lambda_{exc}=601$ nm) of the force-activated chromophore **6c**. We attributed this to the solvatofluorochromism typically observed in such donor-acceptor dye conjugates and generally ascribed to intramolecular charge transfer (ICT).[44]

We then turned towards the PHMA elastomer networks, in which the overall crosslinker amount was 1 mol% of which 0.02 mol% were mechanophores **5a–c**. The low mechanophore content warrants sufficient detectability[23] while leaving the mechanical properties indistinguishable from the parent material.[24] Cube-shaped samples of ca. $2\times2\times2$ mm were obtained by cutting the respective PHMA samples and the cut edges were studied by CLSM. The captured images correspond to a top view on the xy-plane (Figure 2). Wavelengths of the excitation lasers (λ_{exc}) and scanning ranges (λ_{em}) were chosen based on the spectra depicted in Figure 1.

While micrographs of **PHMAa**, allowed localization of bond scission events expectedly (Figure 3a), the advantage of using dual fluorescent mechanophores became immediately visible. For both **PHMAb** and **PHMAc**, the non-activated

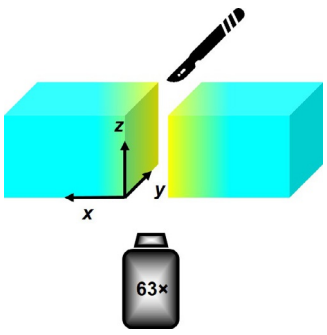

Figure 2. Schematic of a blade-cut sample, and observation of the fluorescence at the respective fracture site (top view of xy-plane) with 63× objective by CLSM.

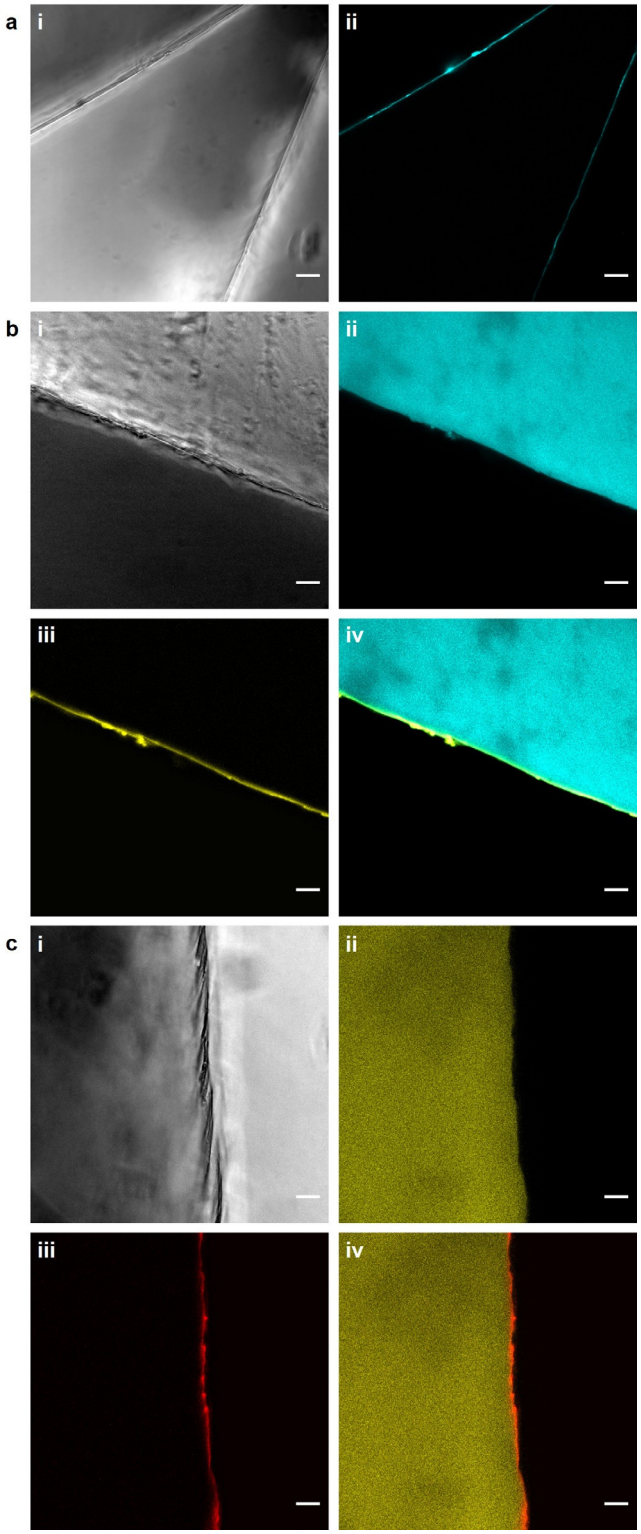

Figure 3. Bright-field images (i), CLSM micrographs (ii, iii), and composites (iv) of the edges of cut PHMA elastomer network samples. a) **PHMAa**; ii) activated mode $\lambda_{exc} = 405$ nm, $\lambda_{em} = 420–500$ nm. b) **PHMAb**; ii) non-activated mode $\lambda_{exc} = 405$ nm, $\lambda_{em} = 420–500$ nm, iii) activated mode $\lambda_{exc} = 470$ nm, $\lambda_{em} = 530–650$ nm. c) **PHMAc**; ii) non-activated mode $\lambda_{exc} = 495$ nm, $\lambda_{em} = 530–650$ nm; iii) activated mode $\lambda_{exc} = 601$ nm, $\lambda_{em} = 616–785$ nm. Scale bar: 20 µm.

mechanophores could be observed in a channel different from that of the activated mechanophores due to their large spectral separation allowing for clear identification of damaged and undamaged areas (Figure 3b,c). While the majority of non-activated mechanophores were localized within the bulk of the samples, the activated mechanophores were in proximity of the cut as product of covalent bond scission. Note here that since the sample was firstly cut with a sharp precision blade and then loaded onto the microscopy slide, the two fluorescent modes at the fracture site portrayed the remaining non-activated and activated mechanophores after cutting rather than the PHMA sample before and after damage was inflicted.

We then reasoned that the dual fluorescent character of the BTD and NTD mechanophores would allow the locally resolved determination of the ratio of non-activated to activated mechanophore and, calibrated with the control compounds, absolute quantification of the number of non-broken and broken crosslinks.

For this, we performed quantitative image acquisition on fractured **PHMAb** with CLSM in photon counting mode (see Supporting Information for detailed procedure). Slicing these micrographs horizontally in *x*-direction led to individual intensity profiles for each pixel line. We hypothesized that due to the inhomogeneous distribution of stress and strain during the fracture of the networks, the number of activated mechanophores varied locally within different areas of the cut. To obtain a representative impression over the measured area, we hence averaged the individual intensity profile slices over the whole *y*-direction yielding an averaged plot profile (Figure 4a). This showed that the fluorescence of the

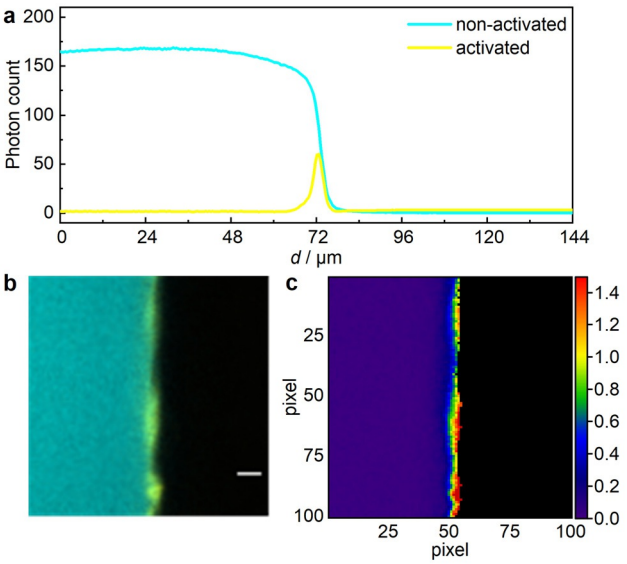

Figure 4. a) Plot profile of non-activated and activated BTD mechanophore at the fracture region of **PHMAb** (300×300 pixel). The number of photons per pixel was vertically averaged over the length of the cut and is shown in dependence of the horizontal distance around the cut. b) Composite of 100×100 pixel CLSM micrographs of non-activated and activated BTD mechanophore. Scale bar: 5 µm. c) Pixel-by-pixel contour map showing the percentage of activated relative to remaining non-activated BTD mechanophores calculated from panel b.

activated BTD mechanofluorophore expanded over a region of 30 pixels (15 μm) from the cut indicating the area affected by the fracture process. Alongside, the non-activated mechanofluorophore intensity plateaued at regions away from the fracture site and then progressively decreased when reaching the fracture site as the signal of the activated mechanofluorophore emerged.

To exclude that the non-uniform activation of the BTD mechanofluorophore over the length of the cut is an artifact of fabrication or measurements, we created a multi-plot profile analysis macro to draw consecutive horizontal selections with a defined distance interval. Applying a region of interest tool and statistics functions, we found that the maximum recorded number of photons for the activated mechanofluorophore locally reached 162, while the number of photons of the non-activated mechanofluorophore neither varied significantly away from nor at the fracture site (exemplary cases in Figure S2). Crosslinked polymer networks are non-ideal, contain dangling chain ends and loops,[45] and mechanophores are differently aligned regarding the direction of macroscopic force application.[46–48] Hence, each pixel volume contained a different number of active mechanofluorophores. However, the above data allowed us to exclude extreme non-uniformity in crosslinker distribution within **PHMAb** pinpointing the variation in activation to microscopic stress and strain distribution differences.

To quantify non-activated and activated mechanofluorophores within fractured **PHMAb**, we then calibrated the CLSM setup by using the photon-counting mode on solutions of the control compounds (Table S2). We chose hexyl acetate as solvent as its refractive index and physicochemical microenvironment matches that of PHMA.[49] This yielded calibration curves for the number of photons per pixel as a function of the concentration of the respective molecule (Table S3, Figure S3). By applying the linear fit equations to convert number of photons to concentrations ($mol\,L^{-1}$), and subsequent multiplication with the Avogadro constant to obtain the number of BTD molecules per m^3, we calculated number densities of the activated mechanofluorophores at their peak intensities at the fracture site of $7.5\times10^{20}\,m^{-3}$ on average, reaching up to $1.9\times10^{21}\,m^{-3}$ locally within the cut. The number density of the non-activated mechanophores was calculated on average to $3.3\times10^{23}\,m^{-3}$ at the fracture site where the activated mechanofluorophore peaked and to $7.3\times10^{23}\,m^{-3}$ within the unaffected bulk. The values measured for the non-activated BTD mechanophore matched the bulk mechanophore number densities of $6.0\times10^{23}\,m^{-3}$ estimated from the synthesis parameters of **PHMAb** and those previously reported for comparable materials.[24] From the 0.02 mol% fraction of BTD mechanophore crosslinks we calculated the overall crosslink density of the network to $7.2\times10^{25}\,m^{-3}$, which was roughly consistent with a value of $6.0\times10^{25}\,m^{-3}$ obtained from swelling experiments and the Flory-Rehner equation (see Supporting Information for detailed procedure).

To further quantify and directly compare the number of mechanofluorophores per confocal volume, we proceeded to z-scanning of sub-diffraction fluorescent beads (see Supporting Information for detailed procedure). According to these calculations, the confocal volume for the non-activated mode was 0.5 μm^3 (close to the typical 0.2 μm^3),[50] while that for the activated mode was 1.6 μm^3. The measured concentrations corresponded, thus, to an average of 1199 and locally up to 3115 activated, and 163441 non-activated mechanofluorophores on average at the fracture site and 366028 non-activated in the unaffected bulk per pixel. The obvious inconsistent total number of mechanofluorophores per pixel was rooted in the decreasing material density at the cut region, since during fracture the free volume increased, and the material thinned and frayed. Förster resonance energy transfer (FRET) between non-activated (FRET donor) and activated (FRET acceptor) BTD mechanophores was ruled out as significant contributor to this phenomenon by calculating the FRET efficiency in **PHMAb** to 0.26% (detailed calculations see Supporting Information).

Subsequently, these data allowed constructing an unprecedented visual representation of the mechanochemical activation process. By calculating the fraction of activated with respect to remaining non-activated mechanofluorophores per individual pixel, we not only provided qualitative bond scission information, but a direct pixel-by-pixel quantification visualization enabled by the dual fluorescent character of the employed mechanofluorophores (Figure 4b,c).

To quantitatively follow fracture in an experimental setup that offers more control than cutting with a blade, we hung weights (85 g and 275 g) on supported notched rectangular **PHMAb** samples inducing fracture by crack propagation at different speeds (Movie S1) and visualized the extent of bond scission in CLSM plot profiles (Figure S4). We observed that a higher weight led to a faster crack propagation and consequently to a higher fraction of activated mechanophores highlighting the potential of this mechanophore system to correlate microscopic bond scission events to the macroscopic mechanical properties of the parent material (Figure S5).

Conclusion

We here presented the design and synthesis of a mechanofluorophore family based on Diels–Alder adducts of π-extended anthracenes and maleimide. The central aromatic moiety of these optical force probes was readily exchanged with dihalide building blocks enabling access to redshifted absorption and emission spectra as well as dual fluorescence. The mechanically induced bond scission process was qualitatively observed in solution by fluorescence spectroscopy and in rubber networks using confocal laser scanning microscopy. In addition, the considerable spectral separation of the emission of non-activated and activated mechanofluorophores allowed the direct and localized quantification of non-broken and broken bonds.

We anticipate that these mechanofluorophores will find more application to analyze the behavior of polymer materials under force in the future, because their dual fluorescent nature allows for tracking of the non-fractured materials, enables to spatially resolve quantification of damage events, and is the basis for their optical tunability over the entire

visible spectrum by comparably straightforward synthesis. We thus expect these mechanofluorophores to contribute to the elucidation of phenomena related to force transduction and dissipation as well as the fracture of materials ranging from soft hydrogels to high-performance polymers.

Acknowledgements

C. B. and R. G. are grateful for support by a Freigeist-Fellowship of the Volkswagen Foundation (No. 92888). M. S. and R. G. acknowledge financial support from an Exploration Grant of the Boehringer Ingelheim Foundation. Parts of the analytical investigations were performed at the Center for Chemical Polymer Technology CPT, which was supported by the European Commission and the federal state of North Rhine-Westphalia (No. 300088302). Financial support is acknowledged from the European Commission (EUSMI, No. 731019). The authors wish to thank F. Meder, L. Witzdam, T. Zensen, S. Folkerts, P. Marten, N. Münstermann, and D. Korkut for their synthetic contributions. Open access funding enabled and organized by Projekt DEAL.

Conflict of interest

The authors declare no conflict of interest.

Keywords: fluorescence · fracture · mechanochemistry · microscopy · polymers

[1] D. R. T. Roberts, S. J. Holder, *J. Mater. Chem.* **2011**, *21*, 8256 – 8268.
[2] F. Ciardelli, G. Ruggeri, A. Pucci, *Chem. Soc. Rev.* **2013**, *42*, 857 – 870.
[3] M. J. Jacobs, K. Blank, *Chem. Sci.* **2014**, *5*, 1680 – 1697.
[4] D. A. Davis, A. Hamilton, J. Yang, L. D. Cremar, D. Van Gough, S. L. Potisek, M. T. Ong, P. V. Braun, T. J. Martínez, S. R. White, J. S. Moore, N. R. Sottos, *Nature* **2009**, *459*, 68 – 72.
[5] J. Li, C. Nagamani, J. S. Moore, *Acc. Chem. Res.* **2015**, *48*, 2181 – 2190.
[6] G. R. Gossweiler, T. B. Kouznetsova, S. L. Craig, *J. Am. Chem. Soc.* **2015**, *137*, 6148 – 6151.
[7] H. Zhang, F. Gao, X. Cao, Y. Li, Y. Xu, W. Weng, R. Boulatov, *Angew. Chem. Int. Ed.* **2016**, *55*, 3040 – 3044; *Angew. Chem.* **2016**, *128*, 3092 – 3096.
[8] Y. Pan, H. Zhang, P. Xu, Y. Tian, C. Wang, S. Xiang, R. Boulatov, W. Weng, *Angew. Chem. Int. Ed.* **2020**, *59*, 21980 – 21985; *Angew. Chem.* **2020**, *132*, 22164 – 22169.
[9] M. J. Teng, X. R. Jia, X. F. Chen, Y. Wei, *Angew. Chem. Int. Ed.* **2012**, *51*, 6398 – 6401; *Angew. Chem.* **2012**, *124*, 6504 – 6507.
[10] Z. Ma, M. Teng, Z. Wang, S. Yang, X. Jia, *Angew. Chem. Int. Ed.* **2013**, *52*, 12268 – 12272; *Angew. Chem.* **2013**, *125*, 12494 – 12498.
[11] Z. Wang, Z. Ma, Y. Wang, Z. Xu, Y. Luo, Y. Wei, X. Jia, *Adv. Mater.* **2015**, *27*, 6469 – 6474.
[12] E. Ducrot, Y. Chen, M. Bulters, R. P. Sijbesma, C. Creton, *Science* **2014**, *344*, 186 – 189.
[13] Y. Chen, A. J. H. Spiering, S. Karthikeyan, G. W. M. Peters, E. W. Meijer, R. P. Sijbesma, *Nat. Chem.* **2012**, *4*, 559 – 562.
[14] Y. Yuan, W. Chen, Z. Ma, Y. Deng, Y. Chen, Y. Chen, W. Hu, *Chem. Sci.* **2019**, *10*, 2206 – 2211.
[15] T. Yamamoto, S. Kato, D. Aoki, H. Otsuka, *Angew. Chem. Int. Ed.* **2021**, *60*, 2680 – 2683; *Angew. Chem.* **2021**, *133*, 2712 – 2715.
[16] T. Kosuge, X. Zhu, V. M. Lau, D. Aoki, T. J. Martinez, J. S. Moore, H. Otsuka, *J. Am. Chem. Soc.* **2019**, *141*, 1898 – 1902.
[17] K. Ishizuki, D. Aoki, R. Goseki, H. Otsuka, *ACS Macro Lett.* **2018**, *7*, 556 – 560.
[18] K. Imato, A. Irie, T. Kosuge, T. Ohishi, M. Nishihara, A. Takahara, H. Otsuka, *Angew. Chem. Int. Ed.* **2015**, *54*, 6168 – 6172; *Angew. Chem.* **2015**, *127*, 6266 – 6270.
[19] C. Löwe, C. Weder, *Adv. Mater.* **2002**, *14*, 1625 – 1629.
[20] A. Lavrenova, D. W. R. Balkenende, Y. Sagara, S. Schrettl, Y. C. Simon, C. Weder, *J. Am. Chem. Soc.* **2017**, *139*, 4302 – 4305.
[21] C. Calvino, A. Guha, C. Weder, S. Schrettl, *Adv. Mater.* **2018**, *30*, 1704603.
[22] T. Matsuda, R. Kawakami, T. Nakajima, J. P. Gong, *Macromolecules* **2020**, *53*, 8787 – 8795.
[23] M. Stratigaki, C. Baumann, L. C. A. van Breemen, J. P. A. Heuts, R. P. Sijbesma, R. Göstl, *Polym. Chem.* **2020**, *11*, 358 – 366.
[24] J. Slootman, V. Waltz, C. J. Yeh, C. Baumann, R. Göstl, J. Comtet, C. Creton, *Phys. Rev. X* **2020**, *10*, 041045.
[25] M. Karman, E. Verde-Sesto, C. Weder, Y. C. Simon, *ACS Macro Lett.* **2018**, *7*, 1099 – 1104.
[26] J. Li, T. Shiraki, B. Hu, R. A. E. Wright, B. Zhao, J. S. Moore, *J. Am. Chem. Soc.* **2014**, *136*, 15925 – 15928.
[27] J. Li, B. Hu, K. Yang, B. Zhao, J. S. Moore, *ACS Macro Lett.* **2016**, *5*, 819 – 822.
[28] E. Izak-Nau, D. Campagna, C. Baumann, R. Göstl, *Polym. Chem.* **2020**, *11*, 2274 – 2299.
[29] R. Göstl, R. P. Sijbesma, *Chem. Sci.* **2016**, *7*, 370 – 375.
[30] D. Yildiz, C. Baumann, A. Mikosch, A. J. C. Kuehne, A. Herrmann, R. Göstl, *Angew. Chem. Int. Ed.* **2019**, *58*, 12919 – 12923; *Angew. Chem.* **2019**, *131*, 13051 – 13055.
[31] E. Izak-Nau, D. E. Demco, S. Braun, C. Baumann, A. Pich, R. Göstl, *ACS Appl. Polym. Mater.* **2020**, *2*, 1682 – 1691.
[32] J. M. Lenhardt, A. L. Black Ramirez, B. Lee, T. B. Kouznetsova, S. L. Craig, *Macromolecules* **2015**, *48*, 6396 – 6403.
[33] S. E. Tan, M. S. Sarjadi, *Polym. Sci. Ser. B* **2017**, *59*, 479 – 496.
[34] J. Du, M. C. Biewer, M. C. Stefan, *J. Mater. Chem. A* **2016**, *4*, 15771 – 15787.
[35] T. C. Parker, D. G. Patel, K. Moudgil, S. Barlow, C. Risko, J. L. Brédas, J. R. Reynolds, S. R. Marder, *Mater. Horiz.* **2015**, *2*, 22 – 36.
[36] Y. Wang, T. Michinobu, *J. Mater. Chem. C* **2016**, *4*, 6200 – 6214.
[37] R. Ratha, A. Singh, M. A. Afroz, R. K. Gupta, M. Baumgarten, K. Müllen, P. K. Iyer, *Synth. Met.* **2019**, *252*, 113 – 121.
[38] B. A. D. Neto, A. A. M. Lapis, E. N. Da Silva Júnior, J. Dupont, *Eur. J. Org. Chem.* **2013**, 228 – 255.
[39] G. Cravotto, E. C. Gaudino, P. Cintas, *Chem. Soc. Rev.* **2013**, *42*, 7521 – 7534.
[40] A. L. Appleton, S. Miao, S. M. Brombosz, N. J. Berger, S. Barlow, S. R. Marder, B. M. Lawrence, K. I. Hardcastle, U. H. F. Bunz, *Org. Lett.* **2009**, *11*, 5222 – 5225.
[41] T. Sato, D. E. Nalepa, *J. Appl. Polym. Sci.* **1978**, *22*, 865 – 867.
[42] M. J. Kryger, A. M. Munaretto, J. S. Moore, *J. Am. Chem. Soc.* **2011**, *133*, 18992 – 18998.
[43] R. Stevenson, G. De Bo, *J. Am. Chem. Soc.* **2017**, *139*, 16768 – 16771.
[44] P. Rietsch, S. Sobottka, K. Hoffmann, P. Hildebrandt, B. Sarkar, U. Resch-Genger, S. Eigler, *ChemPhotoChem* **2020**, *4*, 668 – 673.
[45] L. W. Hill, *Prog. Org. Coatings* **1997**, *31*, 235 – 243.
[46] B. A. Beiermann, S. L. B. Kramer, J. S. Moore, S. R. White, N. R. Sottos, *ACS Macro Lett.* **2012**, *1*, 163 – 166.
[47] A. D. N. Celestine, B. A. Beiermann, P. A. May, J. S. Moore, N. R. Sottos, S. R. White, *Polymer* **2014**, *55*, 4164 – 4171.
[48] B. A. Beiermann, S. L. B. Kramer, P. A. May, J. S. Moore, S. R. White, N. R. Sottos, *Adv. Funct. Mater.* **2014**, *24*, 1529 – 1537.

[49] G. Scott, *Properties of Polymers. Their Correlation with Chemical Structure; Their Numerical Estimation and Prediction from Additive Group Contributions*, Elsevier, Amsterdam, **1992**.
[50] K. Jespersen, Y. Zausjitsyn, S. Westenhoff, T. Pullerits, A. Yartsev, O. Inganäs, V. Sundström, *Fluorescence of Supermolecules, Polymers, and Nanosystems*, Springer, Berlin, Heidelberg, **2008**.

Manuscript received: February 3, 2021
Revised manuscript received: March 23, 2021
Accepted manuscript online: March 30, 2021
Version of record online: May 7, 2021

